

ARTICLE OPEN



In situ microscopic investigation of ion migration on the surface of chromium coated steels

J. Manoj Prabhakar¹✉, Arnoud de Vooy² and Michael Rohwerder¹

Cathodic spreading of electrolyte on two-layers chromium coatings electrodeposited from trivalent chromium electrolyte on steel was studied on the micro- and the macroscale. The behavior is discussed in view of results obtained on electrical conductivity as measured by current-sensing atomic force microscopy. The coatings were found to hinder electron transport. Heterogeneities observed in the electrical conductivity are correlated to heterogeneities of the electrolyte spreading behavior, studied using in situ scanning Kelvin probe force microscopy. In average, the kinetics of spreading observed at microscopic scales are similar to that observed using a scanning Kelvin probe at larger scales. The scanning Kelvin probe force microscopy is demonstrated as a robust in situ technique to follow electrolyte spreading and study microscopic defects/heterogeneities on the surface.

npj Materials Degradation (2022)6:76; <https://doi.org/10.1038/s41529-022-00285-7>

INTRODUCTION

Electrodeposition of chromium from trivalent chromium (Cr^{3+}) electrolyte has gained importance in the recent past with the prerequisite to replace hexavalent (Cr^{6+}) electrolytes from the production process^{1–4}. The process of electrodeposition from Cr^{3+} electrolytes, using trivalent chromium coating technology (TCCT) was found to produce coatings containing chromium, oxygen, and carbon (Cr-O-C)^{4,5}. Carbon and oxygen are incorporated from the organic additives (for example, formic acid) used as complexing agents in the process. These chromium-coated steels are utilized in the packaging industry in conjunction with a polymer topcoat, which can be degraded by cathodic delamination process^{5–11}. Therefore, the cathodic delamination behavior of these polymer coatings on chromium-coated steels has been a topic of extensive research^{5–10}. The cathodic delamination rate of the polymer topcoat was found to decrease with increased oxygen content in the chromium layers^{6,9}, hence the Cr-O-C layer was overcoated with an oxygen-rich Cr-O layer^{5,12}. The two-layers sample with a 12 nm Cr-O topcoat was found to be uniform across the surface, and native oxide was found to be present in the 1.5 nm Cr-O sample at defects, i.e., locations where the Cr-O layer was not deposited⁵. An increasing thickness of the Cr-O topcoat was found to result in reduced delamination rates⁵. The delamination rates of the samples with Cr-O layer thicker than 6 nm were comparable to that of the coatings from Cr^{6+} electrolytes, and the layer was hypothesized to inhibit electron transfer⁵. The migration of cations on the surface of these Cr-O coatings were found to be hindered and driven by the local electrostatic forces on the surface¹⁰.

The kinetics of cathodic electrolyte spreading is similar to cathodic delamination, hence can be a complementary tool to quickly evaluate the role of the metal (oxide) surface on delamination at the metal (oxide)/polymer interface^{10,13}. Figure 1a, b depict the similarity in the mechanisms of cathodic delamination and cathodic electrolyte spreading¹³, respectively. In both the processes, the anodic metal dissolution occurs at the defect where the metal is in contact with the bulk electrolyte. Initially, the cathodic reduction occurs predominantly at the circumference of the defect where the metal/electrolyte interface

is easily accessible to the oxygen. As the electrolyte spreads (Fig. 1b) or enters the degrading metal/polymer interface (Fig. 1a), the cathodic oxygen reduction occurs at these locations (delaminated/ migrated regions and the delamination/migration front). The electrons moving in the metal along the interface/surface from the defect to the front, and the resulting negative hydroxide ions formed by oxygen reduction are compensated by corresponding migration of cations (K^+ in case of KCl) from the defect to the front. At a later stage, when a high concentration of OH^- has accumulated, possibly the hydroxide ions also migrate in the opposite direction, from the front and delaminated/migrated regions to the defect (Fig. 1a, b). Since the mechanism of cathodic delamination and cathodic electrolyte spreading are similar, the potential profile obtained with a scanning Kelvin probe (SKP) during cathodic electrolyte spreading (Fig. 1d), is similar to that obtained during cathodic delamination (Fig. 1c). The transition between lower potentials of the already cation 'migrated' area and the high potentials of the still 'non-migrated' area indicates the migration front in the case of cathodic spreading (Fig. 1d), similar to the delamination front demarcating the delaminated and intact regions in the case of cathodic delamination (Fig. 1c). The potential difference between the delaminated/migrated regions and the intact/non-migrated regions acts as the driving force for the cathodic delamination and electrolyte spreading. Cations will be driven by the resulting electric field into the intact/non-migrated area. As a consequence of this, the potential is pulled down, which will lead to the onset of oxygen reduction reaction (ORR). Both cation migration and ORR play a role in the resulting cathodic delamination or spreading of electrolyte.

In the current work, the conductivity of the chromium coatings is studied using current-sensing atomic force microscopy (CS-AFM) by measuring the local leakage current when a bias is applied. The conductivity is also compared with that of a pure chromium sample with a native oxide layer and an electrolytic chromium-coated steel (ECCS) deposited from the Cr^{6+} electrolyte. The electron transfer across the chromium layer is essential to sustain the oxygen reduction occurring during the cathodic delamination process. CS-AFM or conductive AFM (C-AFM) is a

¹Max-Planck-Institut für Eisenforschung GmbH, Max-Planck-Straße 1, 40237 Düsseldorf, Germany. ²TATA Steel, Research & Development, Ijmuiden Technology Centre, P.O.Box 10.000, 1970 CA Ijmuiden, The Netherlands. ✉email: m.prabhakar@mpie.de

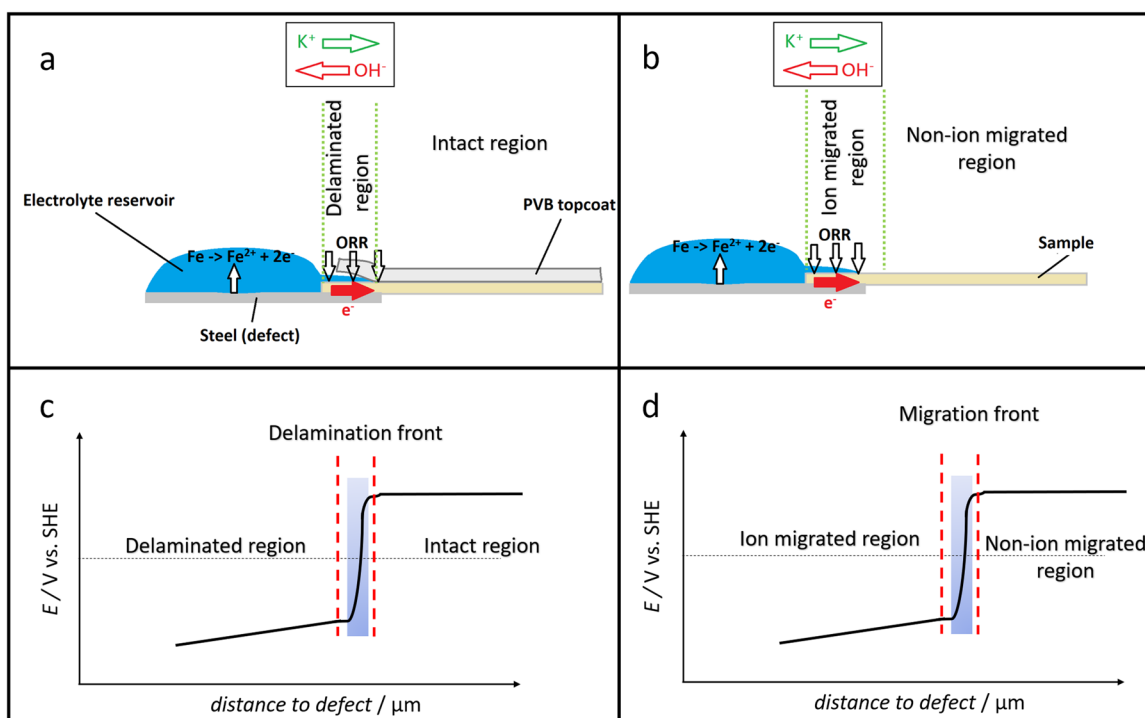


Fig. 1 Mechanism of cathodic delamination and electrolyte spreading. Schematic explaining the mechanisms and regions established during **a** cathodic delamination and **b** cathodic electrolyte spreading. Typical sigmoidal electrode potential (E) vs. distance curves obtained from SKP measurements, depicting various regions established during the progress of **c** cathodic delamination and **d** cathodic electrolyte spreading.

contact mode AFM technique used to characterize local electrical conductivity. The technique is suitable to study samples with low to medium conductivity since it is impossible to obtain a localized conductivity measurement in highly conductive samples^{14–20}. The effect of electrical conductivity on cathodic current for ORR at the polymer-oxide interface is confirmed using phenolphthalein added to the polymer layer. The hydroxide ions resulting from the ORR increase the local pH and lead to the coloration of the pH indicator.

The cathodic spreading of electrolyte on the surface of these chromium-coated steels is studied using in situ scanning Kelvin probe (SKP). Cathodic spreading of electrolyte on the surface of different materials has been extensively studied previously^{21–25}, including very fundamental questions such as oxygen uptake at the electrolyte surface of very thin electrolyte layers to be considered as an important step^{23,26}. In situ SKP measurements were used previously to investigate electrolyte spreading on the surface of steel^{23,25}. Kelvin probe studies on uncovered substrates without polymer coating eliminate the complex surface oxide/polymer interactions and enable the direct investigation of the ion migration kinetics on the surface²⁷. Microgalvanic cells that are formed at the spatially separated cathodic and anodic sites during the cathodic electrolyte spreading can be visualized from the surface potential profiles^{27–29}, as depicted in (Fig. 1d).

The migration of cations at microscopic scales advancing the electrolyte spreading is studied using in situ scanning Kelvin probe force microscopy (SKPFM) technique. The potential profiles obtained from the spreading experiments in the SKPFM are compared with those in the SKP. The electron transfer and ion migration processes occurring at the microscopic scales play an important role in the cathodic delamination behavior. In order to obtain more insight about these processes at the microscopic scale, the surface heterogeneities and their influence on electron transfer and ion migration on these samples are studied using CS-AFM and SKPFM techniques. SKPFM is used to image local surface

potentials with high spatial resolution and works in the non-contact mode of AFM^{30–36}. The potential maps obtained from SKPFM can be used as a key to pinpoint regions that display strong galvanic activity, illustrating a contrast between the cathodic and anodic regions. SKPFM has been used previously to study filiform corrosion^{30–33,37} and cathodic delamination of polymer coatings³⁴. To study cathodic delamination of polymer films using SKPFM, ultra-thin polymer coatings are needed to obtain precise potential signals³⁴. In the current work, the investigation of cathodic spreading eliminates the requirement of a polymer topcoat.

The absence of polymer coating during electrolyte spreading experiments facilitated direct access to the surface for characterization after the experiments. X-ray photoelectron spectroscopy (XPS) was performed on the samples after the electrolyte spreading measurements, to study the distribution of cations on the surface.

RESULTS AND DISCUSSIONS

Current-sensing atomic force microscopy studies

The humidity plays an important role in the meniscus formed between the tip and the sample during CS-AFM measurements^{15,38,39}. Formation of meniscus leads to decreased resolution in the conductivity maps due to the pick-up of leakage current from a larger area than from a localized point. In all the measurements carried out in this study, a very low relative humidity (12–15% RH) was maintained. The conductivity maps obtained from spatially mapping the leakage current for an applied bias of 2V are shown in Fig. 2. The pure chromium with native oxide layer displayed leakage current from 94% area of the surface at the applied bias of 2V (Fig. 2a). The ECCS sample displayed almost no leakage current (Fig. 2d), and the sample 10C-120 showed leakage current only from 2% area of the surface (Fig. 2c). A mixed behavior is observed for the sample 10C-1.50, with a

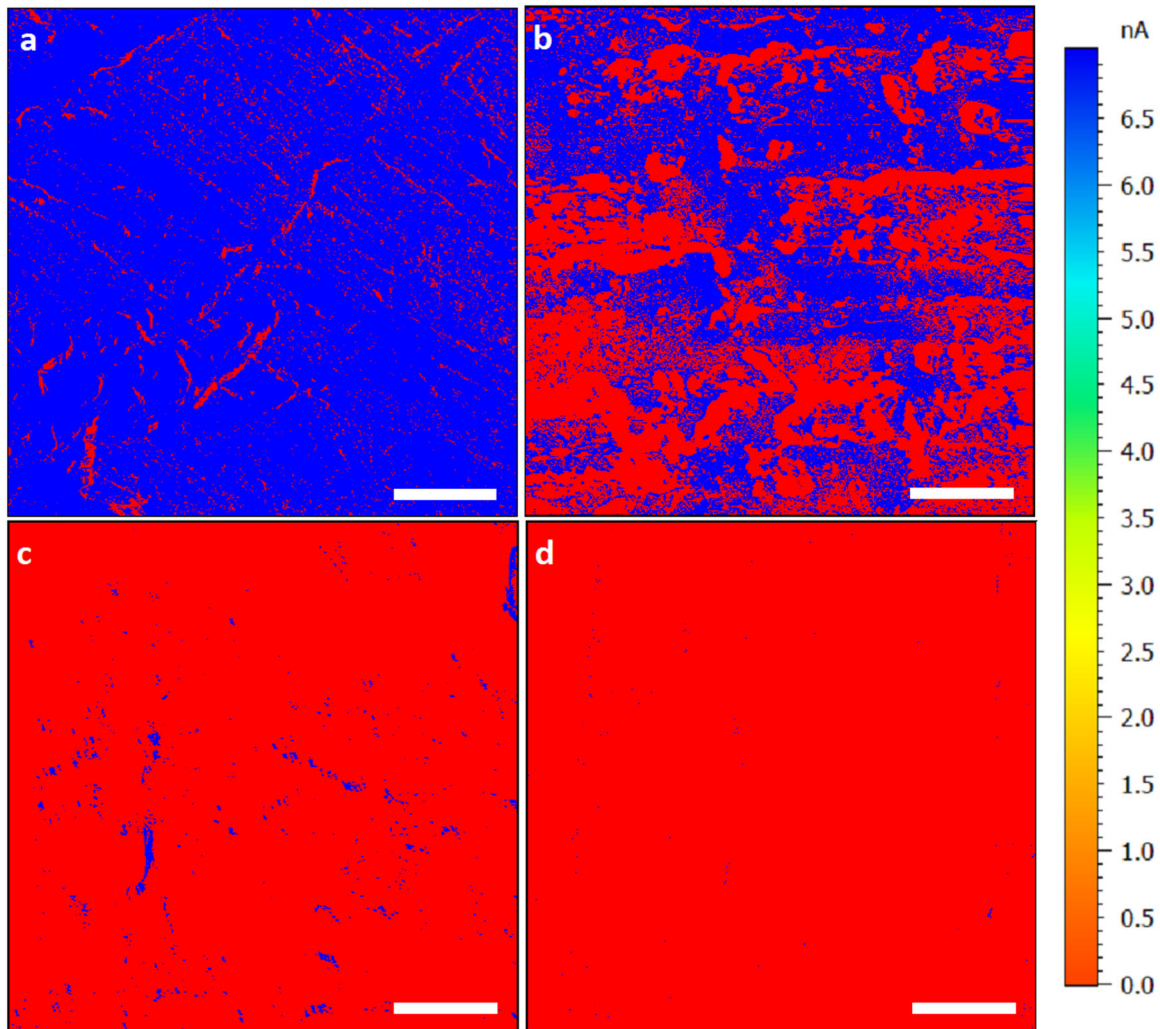


Fig. 2 Conductivity maps at 2 V bias applied to the AFM tip for samples. **a** Pure Cr with native oxide, **b** 10C-1.5O, **c** 10C-12O, and **d** ECCS. The scale bars in **a**, **b**, **c**, and **d** indicate 10 μm .

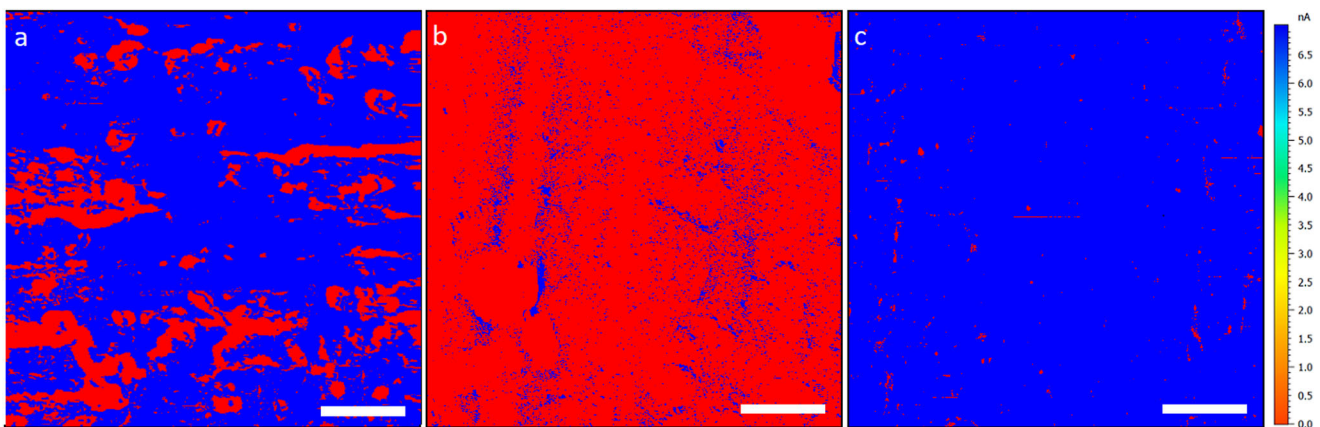


Fig. 3 Conductivity maps at 8 V applied bias for samples. **a** 10C-1.5O, **b** 10C-12O, and **c** ECCS. The scale bars in **a**, **b**, and **c** indicate 10 μm .

48% area of the surface displaying leakage current (Fig. 2b). It is evident from the images that the electrodeposited TCCT (10C-12O) and ECCS layers are highly resistive to the flow of current. The resistive nature of the TCCT with Cr-O layer is evident from the mapping of leakage current at 8 V applied bias, as depicted in Fig. 3. Even at such high applied bias, the sample 10C-12O showed

very few conductive regions (Fig. 3b). In contrast, the ECCS sample became completely conductive at this high applied bias (Fig. 3c). The sample 10C-1.5O still showed mixed behavior, with 75% of the locations conducting current (Fig. 3a). This behavior of the sample 10C-1.5O can be attributed to the non-uniform deposition process at such low Cr-O layer thicknesses. It was reported previously that

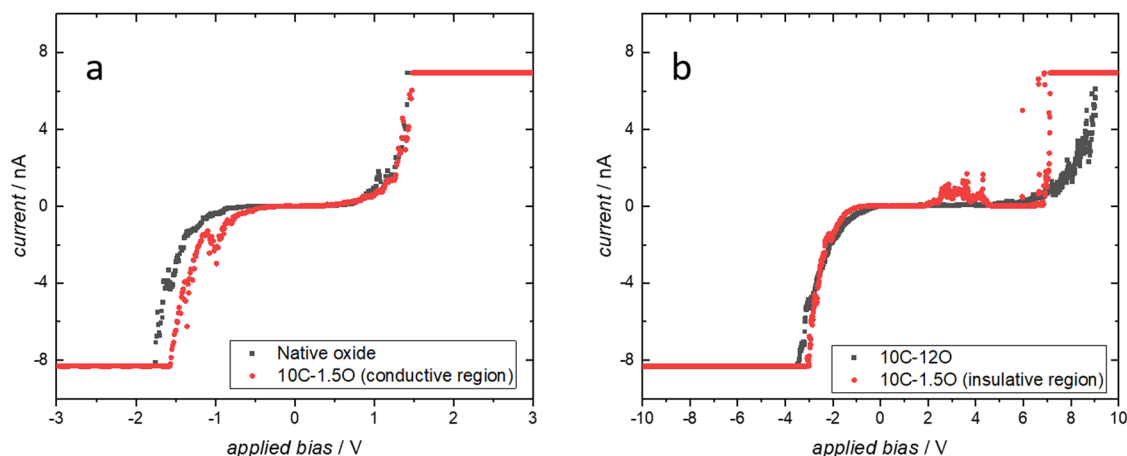


Fig. 4 Current–voltage sweeps obtained from different locations on the samples. Current–voltage sweeps obtained from the **a** conductive regions of the 10C-1.5O and native oxide on chromium samples and **b** non-conductive regions of the 10C-120 and 10C-1.5O samples.

a native chromium-oxide layer is formed on the sample 10C-1.5O at the regions where the deposition of the Cr–O layer does not occur⁵. It seems reasonable that the regions on the sample with the native oxide are where leakage current is observed, whereas the Cr–O covered regions display no conductivity. The non-spontaneous nature of the electrodeposition process from trivalent chromium electrolyte leads to a porous structure^{8,40} and a layer incorporated with iron⁸. The few conductive regions in the sample 10C-120 could arise from such defective regions of the Cr–O layer.

Figure 4a, b depict the current–voltage sweep (I – V) curves obtained from the conductive and non-conductive regions, respectively. A sample behaving as an ohmic conductor shows a linear relationship between the leakage current and applied potential⁴¹. A rectifying or semiconductive behavior displays a zero current region characteristic of the band-gap⁴¹. The band-gap energy is derived from the zero current region in the I – V curve^{19,20}. All the I – V curves obtained in this study illustrate a distinct rectifying behavior. The similar I – V curves obtained from the conductive regions on the sample 10C-1.5O and the chromium sample with native oxide (Fig. 4a) reaffirm the formation of native oxide on the sample 10C-1.5O at locations where the Cr–O layer is not deposited. The asymmetry in the positive and negative bias regions of the I – V curves indicate the type of semiconductor^{42,43}. Rectifying behavior is observed when a Schottky barrier is produced at the contact between the tip and the sample. The contact is forward biased at negative voltages for an n-type semiconductor⁴³. Therefore, a larger zero current region in the positive bias denotes n-type semiconductor behavior and vice-versa for a p-type semiconductor. The native oxide layer on the pure chromium sample displays a marginally higher zero current in the negative bias (Fig. 4a), indicating a p-type semiconductor behavior, as expected for chromium oxide⁴⁴.

The semiconductive behavior is more obvious on the Cr–O layer on the samples 10C-120 and the non-conductive regions of the 10C-1.5O sample (Fig. 4b). The curves obtained from the Cr–O layer exhibit a higher zero current region in the positive bias, characteristic of an n-type semiconductor. The oxide in the Cr–O layer was reported to be a metastable oxide deficient in oxygen⁵. Metallic oxides that contain excess metal or are deficient in oxygen are expected to exhibit n-type semiconductor⁴⁵, with the excess electrons from the metal occupying the states that are close to the conduction band minimum. The n-type Cr–O oxide was also found to readily adsorb oxygen on the surface, resulting in a band bending upwards, leading to inhibited electron transport¹⁰. The oxygen-deficient oxide in the Cr–O layer can thus be inferred as an n-type semiconductor, with huge resistance

to electron conductivity across it. The oxide was already previously hypothesized to inhibit the transfer of electrons required to sustain the ORR occurring during cathodic delamination⁵. In the current study, the electron conduction behavior has been systematically studied using CS-AFM, verifying the proposed hypothesis.

Observations with phenolphthalein

During cathodic delamination of a polymer from a metallic substrate, the anodic metal dissolution occurs at the defect where the substrate is in contact with the electrolyte. A part of the corresponding cathodic reaction (ORR) occurs at the delaminated regions and the delamination front⁴⁶. The ORR occurring during cathodic delamination results in increased pH at the delaminated and delaminating interface. The resulting alkaline pH can be monitored visually by the coloration of phenolphthalein. Various photographs depicting the coloration of phenolphthalein with the progress of delamination on the PVB-coated 10C-1.5O, 10C-120, and pure chromium samples are shown in Supplementary Fig. 1. The ORR is vigorous on the surface of 10C-1.5O and pure chromium samples, as observed by the violet coloration of the pH indicator. No coloration was observed in the delaminated regions on the 10C-120 sample even after 2 weeks. The lack of coloration does not indicate a complete absence of ORR. It can be elucidated that the current density for oxygen reduction is stifled, leading to diminished hydroxide ion concentration. The number of hydroxide ions formed might be insufficient to result in the coloration of the pH indicator. This inhibited oxygen reduction is supported by the suppressed electron transfer across the Cr–O layer reported in the previous section.

Cathodic electrolyte spreading

During electrolyte spreading, several secondary microdroplets were found to initiate from the anodic primary droplet as a consequence of ORR occurring in the migrated area and corresponding further migration of cations towards the migration front to maintain charge neutrality^{21–23}. The microdroplets were found to be highly alkaline and enriched with cations (Na^+). Oxygen reduction occurring on the surface was followed by using phenolphthalein on the surface²³ and was found to initiate at the circumference of the primary droplet and spread outwards. The concentrated NaOH solution formed as a result of ORR and the cation migration promotes the diffusion of water from the edge of the droplet to dilute the solution²³. This leads to the spreading of the droplet. The uptake of water is, of course, not only from the bulk of the electrolyte, but also from the environment, which was

supported by changing rates of spreading with change in humidity²³.

The spreading of the electrolyte can also be explained with respect to the surface tension acting on the droplet. The charge on the surface of an oxide-covered metal is determined by the prevalent local pH at the surface. The pH at which the net charge on the surface is zero is termed as the isoelectric point (IEP) or zero point of charge (ZPC)⁴⁷. As the pH on the surface deviates from this point, the affinity of water to the surface increases due to the resulting charge on the surface⁹. The interfacial tension at the electrolyte-oxide interface is the highest at IEP and lower as the pH at the surface deviates further from the IEP⁴⁸. At high pH values prevalent at locations where oxygen reduction has occurred, the surface charge density is higher since the deviation from IEP is higher. At such locations with high prevalent alkaline conditions, interface tension is lower and the spreading of the droplet is enhanced. Migration of anions is mitigated due to the negatively charged surface, at pH values higher than the IEP. The models discussed above, explaining cathodic electrolyte spreading on the surface of a material, are analogous to the cathodic delamination mechanism prevalent when the material is coated with a polymer. It is pointed out here that for electrolyte spreading to happen, first cation migration has to occur, which pulls down the potential, thus initiating oxygen reduction, which is analogous to cathodic delamination^{10,49}.

In the current section, the cathodic spreading on the surface of the samples is studied using in situ SKP and SKPFM measurements. The kinetics of spreading of the electrolyte is compared with that of cathodic delamination studied previously⁵.

Scanning Kelvin probe studies. Figure 5 depicts the evolution of electrode potential (E) profiles as a function of distance from the defect, during the progress of the spreading of the electrolyte. The profiles result in three distinct regions as the spreading progresses (as depicted in Fig. 1c) and are similar to the ones obtained during cathodic delamination on the PVB-coated samples reported previously⁵. As the spreading of electrolyte progresses, a front of migration is formed separating the ion migrated region (lower potentials close to the potential of the defect) from the non-migrated region (higher potentials). This is identical to the delamination front separating the delaminated and intact regions, formed during cathodic delamination. The rate of spreading of the electrolyte is studied by plotting the position of this front with time. The rate of spreading of the electrolyte is comparable to the rate of delamination of the PVB coating for each sample (Fig. 6). A similar observation was reported previously, where the ion transfer kinetics on iron were found to be similar on a polymer-coated, highly defective polymer-coated, and uncovered surface^{27,28}.

The potentials of the intact regions in the presence of PVB coating in the previous study⁵ are also identical to the potentials measured on bare substrates in this study. A difference in potential in the presence of a polymer coating compared to the bare surface was suggested as a non-destructive method to study the bonding between the polymer and the surface^{50,51}. A partial electron transfer occurs from the basic functional group to the acidic group. For example, the charge transfer between a polymer coating with basic functional groups and an acidic oxide on the surface leads to a dipole at the interface with a negative charge towards the surface of the oxide and a positive charge towards the polymer film. This would result in a decrease in the work function of the substrate and hence a decrease in potential. The higher the shift in potential, the stronger the acid-base interactions and dipoles at the interface. For the case of different oxides on steel, a higher decrease in the potential after coating with a polymer was demonstrated to result in better adhesion by the formation of stronger interfacial bonds⁵⁰. In the current study, a potential of the bare substrate similar to that of PVB-coated

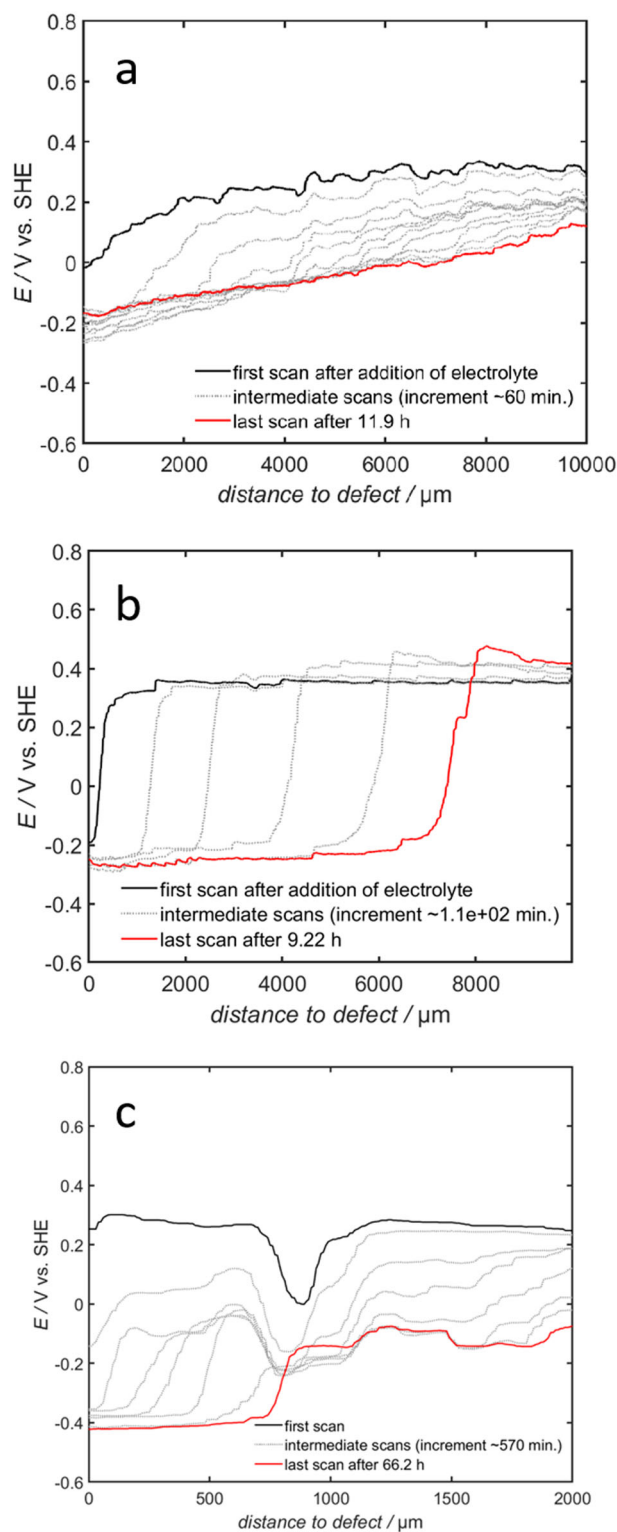


Fig. 5 Potential (E) vs. distance profiles obtained at various times during the progress of electrolyte-induced cathodic spreading on samples. **a** Chromium with a native oxide layer, **b** 10C-1.5O, and **c** 10C-12O.

surface is expected due to the weak bonding nature of PVB to the surface.

However, independent of adhesion, also pre-treatments on the surface that would reduce the potential of the intact interface would lead to lower delamination rates^{52–55}. Such pre-treatments

inhibit the oxygen reduction kinetics even at more cathodic potentials, as expected from a more negative potential at the intact interface. In the current study, it is evident that the sample with a thicker Cr–O layer (10C-120) has a lower potential at the non-migrated regions (Fig. 5c) compared to the 10C-1.50 sample (Fig. 5b). The oxygen reduction kinetics is therefore more retarded in the presence of the thicker Cr–O layer, as confirmed by the lack of coloration observed using phenolphthalein in the PVB topcoat and inhibited electron transfer from the CS-AFM measurements. The retarded ORR kinetics seem to fit well with a lower rate of cathodic delamination or electrolyte spreading, as also anticipated

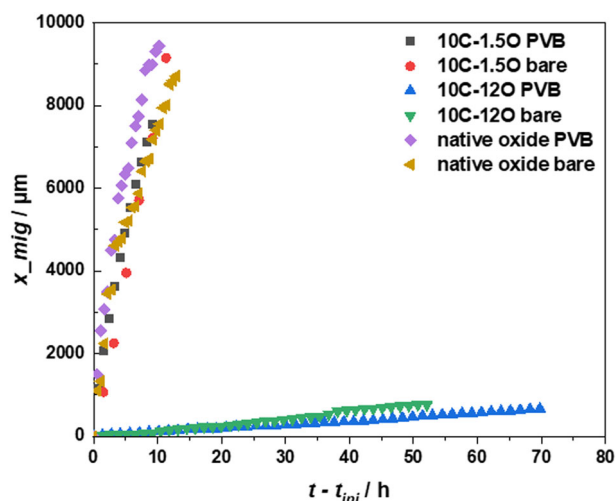


Fig. 6 Position of migration front vs. time plot for different samples. Position of migration front (x_{mig}) plotted as a function of time for the bare and PVB-coated samples.

from the smaller driving force (difference in potentials at the delamination/migration front).

Scanning Kelvin probe force microscopy studies. The formation of microscopic galvanic elements is investigated using in situ SKPFM measurements. Soon after placement of the electrolyte droplet, visible contrast in the electrolyte spreading behavior of the samples 10C-1.50 and 10C-120 could be distinguished as depicted in the photographs in Supplementary Figs. 2 and 3. The primary droplet on the sample 10C-120 remained intact for 24 h after initiating the electrolyte spreading measurements. On the contrary, secondary droplets were formed and grew in size soon after the initiation of the measurements in the sample 10C-1.50. A similar observation of the growth of microdroplets was previously reported in the case of 0.5 M NaCl droplet on carbon steel²³. The observed behavior can be explained according to the model for cathodic spreading described earlier in Introduction. The inhibited ORR on the sample 10C-120 due to the hindered electron transfer kinetics leads to reduced cation migration to the edge of the droplet, where it would be otherwise needed for supporting the ORR in the meniscus region, resulting in highly retarded electrolyte spreading. In sample 10C-1.50, where the cathodic reaction is not as hindered as in the sample 10C-120, the increased pH at the edge leads to a larger deviation from the IEP. This results in decreased surface tension of the droplet, and thus enhanced spreading. The secondary droplets are formed when water moves to the cation migrated regions to dilute the highly alkaline electrolyte formed by the hydroxide ions formed during ORR²³. Again it should be noted that the electrolyte spreading is advanced by initial cation migration. The cation migration then initiates ORR, which results in the pH change and thus spreading.

A series of high-resolution potential images obtained during in situ cation migration on the surface of the sample 10C-1.50 are shown in Fig. 7. The first scan (Fig. 7a) was commenced immediately after initiation of the electrolyte spreading

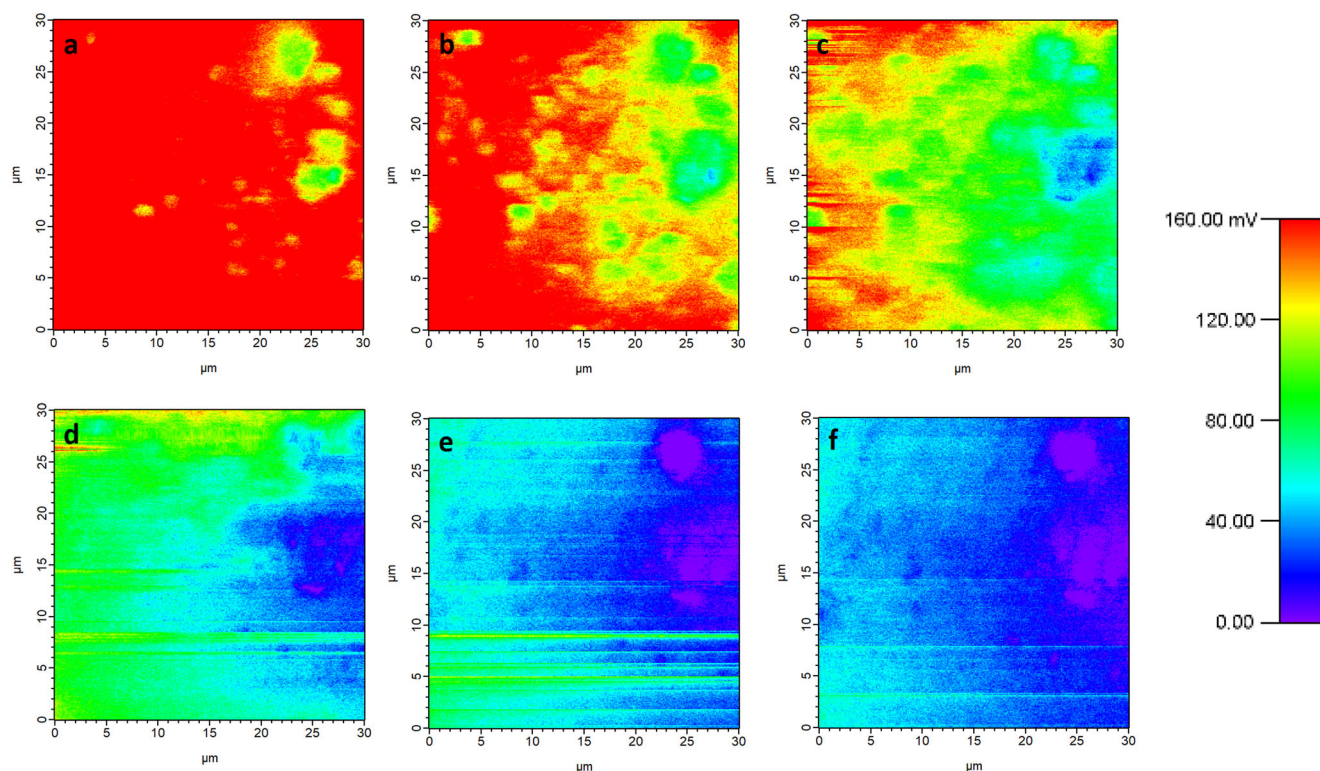


Fig. 7 High-resolution electrode potential mappings obtained during in situ cation migration on the surface of the sample 10C-1.50 at different times. **a** 0 min (first scan after placing the electrolyte droplet), **b** 8 min, **c** 16 min, **d** 24 min, **e** 48 min, and **f** 80 min.

measurement and a few micrometers ahead of a secondary droplet. From the potential maps in Fig. 7a–f, it is clear that the cation migration advancing the electrolyte spreading evolves mainly through discrete ‘sites’ (where the potentials are quickly reduced, turning blue in Fig. 7). These sites most likely are correlated to the conductive native oxide grown on the surface of the sample where the Cr–O layer is not deposited (Figs. 2b and 3a). Interestingly, the potential on these sites gets lower than the surrounding area, i.e., the cation migration to these site occurs partly against the electric field (note that the potential gradient experienced by the cation is inverse of the gradient in the electrode potential^{49,56}). Since the decrease in potential is correlated by an accumulation of cations, it seems also to occur against the gradient of the cation concentration on the surface. It is hence proposed that the chemical potential of the cations on these sites is much lower than the one on the Cr–O layer, which would provide a corresponding gradient in electrochemical potential even at opposed gradients of potential and concentration. These sites are hence the preferred locations where the potentials are reduced initially and oxygen reduction is initiated, followed by a decrease in potentials in the surrounding regions. Thus, these regions act as preferred locations for the occurrence of oxygen reduction reaction and the correlated continuous migration of cations to these regions to compensate for the negative hydroxide ions produced. Hence from these sites the migration of cations subsequently spreads also into the surrounding areas (as can be seen in Fig. 7).

The potential profiles extracted from these maps along a line parallel to the horizontal axis, at vertical axis position of 18 μm are presented in Fig. 8. It should be emphasized that the potentials obtained using the SKPFM are not absolute values, unlike the values obtained from the SKP, which are calibrated. The potential profiles obtained from the SKPFM depict local heterogeneities on the surface potentials at the microscopic scale, due to the native oxide and the deposited Cr–O. Different from the results obtained by SKPFM, the potentials obtained on the sample 10C-1.5O from the SKP are quite homogenous at locations where the electrolyte spreading did not occur (Fig. 5b). This is because the SKPFM technique is better resolved compared to the SKP where a tip of $\sim 120\ \mu\text{m}$ diameter is used, leading to an averaged surface potential value in the SKP. However, a clear migration front as observed in the SKP is not visible in the profiles obtained by SKPFM for the sample 10C-1.5O. This is because of the small scanned area and the fast cation migration kinetics on the sample,

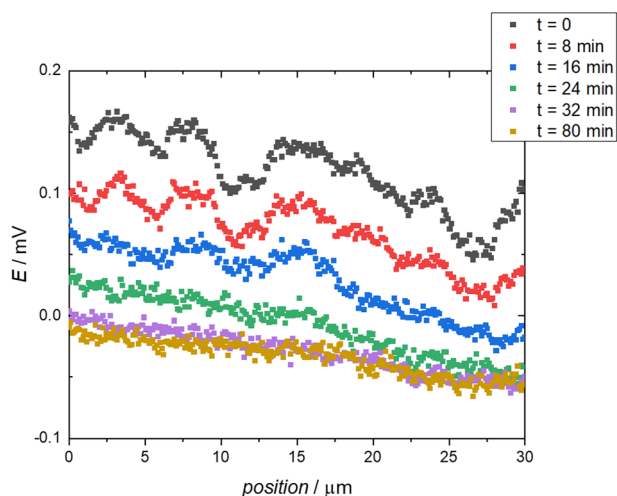


Fig. 8 Surface potential profiles extracted from the maps on the sample 10C-1.5O. Surface potential (E) vs. horizontal axis position, extracted from the SKPFM images in Fig. 7 at a vertical axis position of 18 μm .

which leads to a virtually uniform reduction in the potential across the entire scanned area.

Figure 9 depicts a series of high-resolution electrode potential images obtained during in situ electrolyte spreading on the surface of the sample 10C-12O. There was no observable difference in the potentials for several hours since the onset of the electrolyte spreading measurement and hence the initial scans are not displayed here. The first displayed scan (Fig. 9a) was commenced after 4.2 h of placing the electrolyte and very close to the primary electrolyte droplet. A clear front distinguishing the cation migrated region (depicted by low potentials or blue color in Fig. 9) from the non-migrated region (depicted by the green or red high potential region in Fig. 9) is noticeable from the potential maps. Though the sample 10C-12O consists of an evenly deposited Cr–O layer⁵, a disparity in the cation migration behavior is observed at different locations of the sample. For instance, the migration appears to be faster along the top edge (vertical axis value $\sim 18\ \mu\text{m}$) when compared along the line with vertical axis value $\sim 6\ \mu\text{m}$. To investigate the heterogeneous behavior, the surface potential profiles along these lines (vertical axis values 18.75 μm and 6.51 μm) were extracted from the maps and are depicted in Fig. 10a, b, respectively. The curves in Fig. 10a are comparable to the evolution of potentials observed using the SKP, exhibiting a sharp migration front that advances as the electrolyte spreading progresses. The difference in potentials of migrated and non-migrated regions observed in the SKPFM are also comparable to the difference observed in the SKP. In an earlier work on in situ monitoring of cathodic delamination by SKPFM, it was reported that this absolute drop in potentials at the delamination front observed in the SKPFM maps was smaller in comparison to that observed in SKP³⁴. The difference was assumed to arise because of the delamination front spreading over a larger area in the SKP and thus only a fraction of the potential drop resulted in the small area measured in the SKPFM. It was also assumed that the sharp potential drop observed in the SKPFM could be smeared out in the SKP due to lower resolution, resulting in a gradual increase in potential in the delaminated region. In this study, the potential drop at the front is comparable, indicating that most of the segments of the front exist within the region scanned in the SKPFM for the 10C-12O sample. This supports that the SKP leads to a significant smearing out of the potential profile at the front. It also indicates that the potential profile at the front is here much sharper than in those earlier experiments³⁴, and the whole drop of potential across the front is observable within the small scan window of SKPFM. This is different from the scans shown in Fig. 7, where only a small drop is observed, which is much smaller than the one observed in SKP. The potentials of the non-migrated regions are uniform on the sample 10C-12O, in contrast to the potentials in the sample 10C-1.5O (Fig. 8). This is attributed to a uniform Cr–O layer on the 10C-12O sample compared to a spatially distributed Cr–O and native oxide layers on the sample 10C-1.5O⁵.

The dissimilar cation migration profiles in Fig. 10a, b could be correlated to the heterogeneities observed on the 10C-12O sample in CS-AFM (Figs. 2c and 3b). The electrical conductivity was found to be enhanced at certain regions on the samples, which were attributed to defects in the Cr–O layer. The defects could be iron inclusions or nanopores exposing chromium underneath the Cr–O layer, which are characteristic of the electrodeposition process^{8,40}. These regions of higher conductivity will be the locations where the cathodic oxygen reduction reaction is less hindered. Furthermore, the surface termination was found to be different in the Cr–O-coated regions due to the adsorption of oxygen resulting in a $\text{O}^{\delta-}$ -terminated surface¹⁰. The mobility of cations migrating from regions of lower potential to regions with higher potential can be expected to be different for the Cr–O-coated regions and the defective regions. Since the cation migration on the native oxide surface is much faster than on the Cr–O covered samples (as can be seen in Figs. 5 and 6), it is reasonable to assume that on areas rich in native oxide both cation

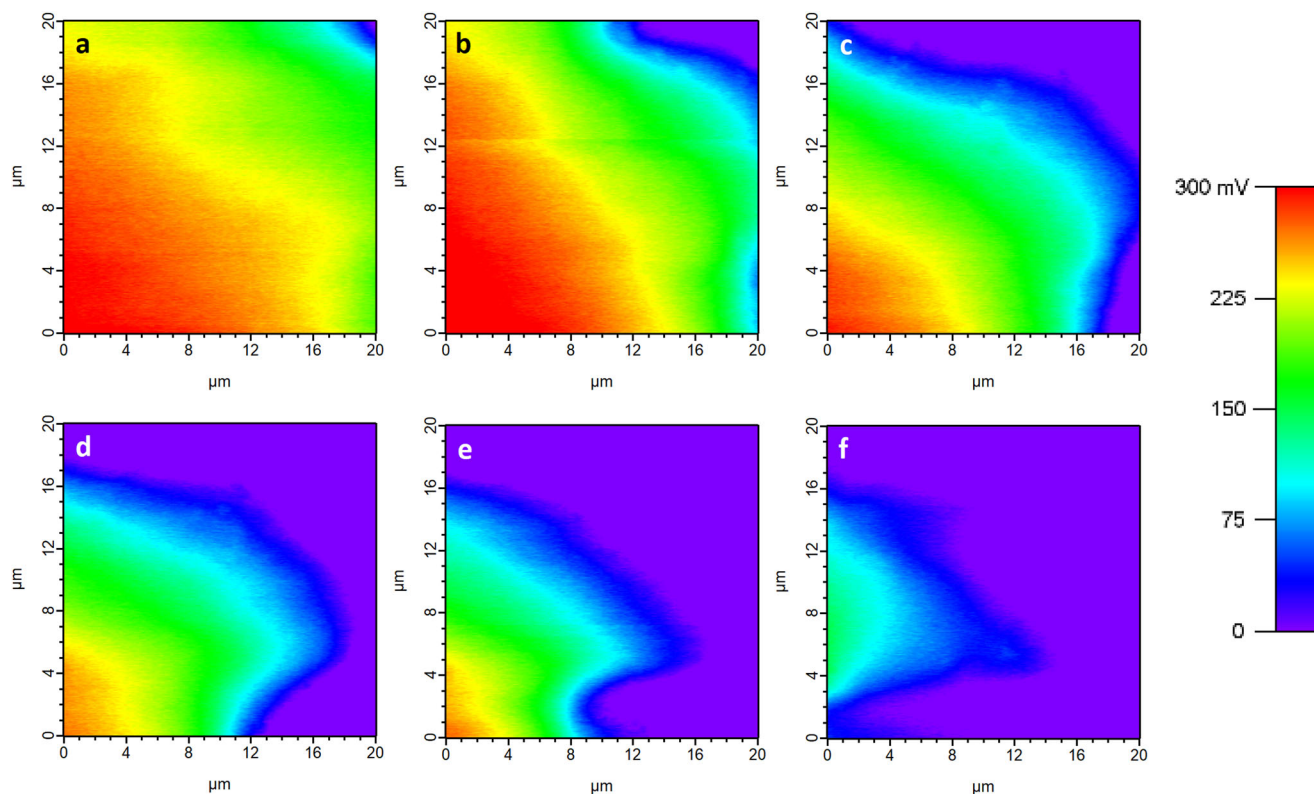


Fig. 9 High-resolution electrode potential mappings obtained during in situ electrolyte spreading on the surface of the sample 10C-120 at different times. **a** 0 min (4.2 h after placing the electrolyte droplet), **b** 16 min, **c** 32 min, **d** 48 min, **e** 64 min, and **f** 112 min.

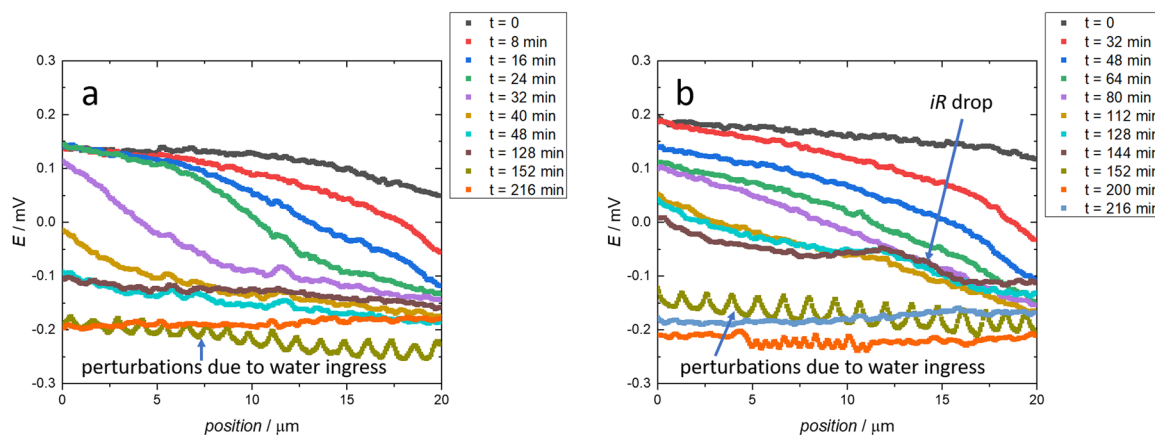


Fig. 10 Surface potential profiles extracted from the maps on the sample 10C-120. Electrode potential (E) vs. horizontal axis position, extracted from the SKPFM images in Fig. 9 at a vertical axis position of **a** 18.75 μm (defective Cr-O) and **b** 6.51 μm .

migration as well as oxygen reduction kinetics are at a much higher rate than on the Cr-O modified surface areas. No contrast in potential is observed on the non-migrated regions of the 10C-120 sample. Hence, it is assumed that the defective areas are rather regions where the Cr-O layer is quite defective but still present, rather than the exposure of underlying Cr-O-C layer like in the case of the 10C-1.50 sample. The progress of the cation migration observed at these more defective areas is therefore still much slower than on the native chromium oxide. The potential is decreased (Fig. 10a) in the regions where cations have migrated (characterized by lower/cathodic potentials), and ORR occurs. It is proposed, in accordance with observations made in an earlier work⁵⁷, that a higher pH at the surface leads to more fixed negative groups, resulting in a higher cation mobility. For areas where oxygen

reduction reaction is inhibited, less OH^- is accumulated, which leads to a significant decrease in cation mobility. Since the mobility of cations on the native oxide rich surface is already higher right from the beginning and it is further enhanced by ORR, and it is expected hence both are also higher on the more defective Cr-O surface, no discernible potential drop (iR) is caused there by the ion migration necessary to support the oxygen reduction in the migrated area and at the front. Hence, nearly the full potential drop between the migrated and non-migrated surfaces is available as the driving force for advancing the cation progress at the front. On the Cr-O-coated areas in the migrated region, on the other hand, a large iR drop can be seen (marked in Fig. 10b). The cathodic current (i) observed on the 10C-120 sample is very low, as was ascertained from the observations using phenolphthalein. The iR drop can therefore be

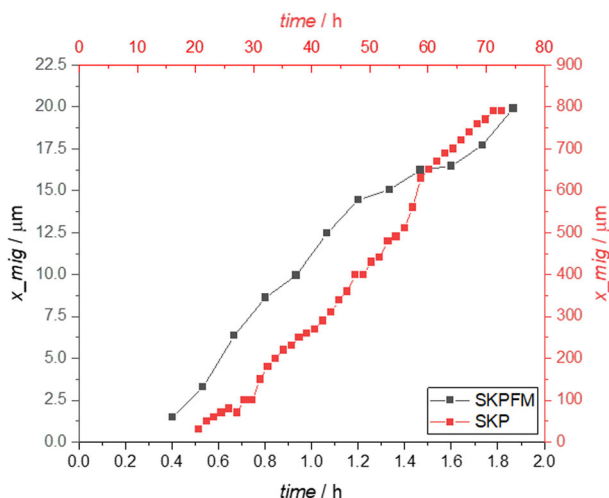


Fig. 11 SKP vs. SKPFM comparison. Position of the front of migration (x_{mig}) vs. time obtained from the scanning Kelvin probe (SKP) and scanning Kelvin probe force microscopy (SKPFM) measurements during cathodic electrolyte spreading on 10C-12O.

inferred to be arising due to the resistance (R) to cation migration in these Cr–O-coated locations, due to the local electric fields on the surface¹⁰. The established iR drop was observed to exist until 144 mins (Fig. 10b), while the migration was already completed by 44 min in the surrounding regions (Fig. 10a). Though the spreading of water droplets on the sample 10C-12O was not visually observed (Supplementary Fig. 3), water was found to accumulate after the cation migration was completed, which led to perturbations in the scans (marked in Fig. 10a, b). The ingress of water into the cation migrated regions is also evident from the 3-dimensional potential-topography maps of the sample (Supplementary Fig. 4g). Supplementary Fig. 4a–g displaying the 3D topography also demonstrate that the drift in the sample during the entire course of the experiment was negligible. The diffusion of water led to homogenization of potentials across the entire surface and the iR drop faded away (Fig. 10b after 152 min). The current investigation of electrolyte spreading using SKPFM substantiates the models proposed previously^{21–23}, illustrating the migration of cations followed by the accumulation of water.

The faster ion migration in the regions with supposedly defective Cr–O layer is hence explained by the faster ion migration kinetics, and also by the steeper potential gradient at the front. This is resulting from the absence of an iR drop in the already migrated area, leaving a higher difference in potentials at the sharper migration front, which increases the driving force for cations to migrate onto the yet non-migrated surface.

The position of the migration front (x_{mig}) as a function of time for the electrolyte spreading measurements carried out on the sample 10C-12O in the SKP (Fig. 5c) and SKPFM (Fig. 10b) are plotted in proportional scales in Fig. 11. It is assumed that the microscopic regions where the cation migration is the slowest (in the SKPFM) control the overall rate of migration in the macroscopic scale (in the SKP). Therefore, the position of the migration front obtained from migration at vertical axis position of 6.51 μm (slower progress, Fig. 10b) is plotted in Fig. 11. It is evident that the rate of migration (slope of the curve) is similar in both cases, establishing the SKPFM technique as a robust in situ technique to study electrolyte spreading and capable of identifying heterogeneities at the microscopic scale.

XPS studies

XPS survey scan spectra were obtained from locations at different distances from the defect, on the chromium with native oxide, 10C-1.5O and 10C-12O samples after the cation migration

measurements. The XPS measurements were carried out on the chromium and 10C-1.5O samples soon after the cation migration measurements in the SKP (Fig. 5a, b). The sample 10C-12O in contact with the electrolyte was placed in an external humidity chamber for 2 weeks before XPS measurements, to further sustain the spreading on the surface, so that the cations migration proceeded to more than 5 mm. The cation concentrations quantified from the spectra obtained at different locations are plotted in Fig. 12a. The concentrations of cations close to the defect are lower than the concentrations close to the migration front (close to the position of 10 mm from the defect on the samples 10C-1.5O and chromium, and around 5 mm on the sample 10C-12O). The cations migrate along the surface of the sample and thus are causing the observed decrease of potential. Furthermore, once oxygen reduction is initiated and occurs, further cation migration has to occur for counterbalancing of the hydroxide ions produced by ORR. This should result in a continuous accumulation of cations in the migrated regions where ORR has to be sustained to keep the potential at the observed low levels. On the contrary, lower cation concentration in the migrated region compared to the migration front is observed on all the three samples. This could indicate a possible migration of hydroxide ions from the regions where ORR occurs towards the defect, in addition to the migration of cations from the defect to the regions where ORR occurs (as depicted in Fig. 1). In fact, it seems that cation migration mainly serves to initially pull down the potential. Once oxygen reduction occurs, the ion flow for closing the electric circuit (electron flow from the defect to the migrated surface being one half of the circuit) thus is provided by the hydroxide ion flow from the migrated area towards the defect.

From Fig. 12a it is also evident that the concentration of cations in the migrated regions is higher in the chromium sample with native oxide (~10–12 at.%) than in the migrated regions of the samples 10C-1.5O (~2–6 at.%) and 10C-12O (~2–3 at.%). This is suggested to be due to a higher capacitance of the sample with the thinner Cr–O layer. Thus, lesser cations are needed to pull down the potential to a similar level for the 10C-12O than for the 10C-1.5O. It was previously proven that the Cr–O oxides readily adsorb oxygen, resulting in a partial negatively charged $\text{O}^{\delta-}$ termination on the surface¹⁰. This should lead to a quick expulsion of the produced hydroxide anions towards the defect, which implies that the ion flow to sustain ORR in that case occurs exclusively by OH^- migration towards the defect. This might also explain why the cation concentration is much lower in the migrated area of 10C-1.5O than of the Cr sample covered by native oxide. Note that the capacitance seems to be similar for the two cases, as the cation concentration at the front is similar, too.

Hence it is postulated here that when the generated hydroxide ions are ejected from the migrated regions where the ORR occurs towards the defect (Fig. 1), accumulation of cations in the migrated regions no longer occurs. To ascertain this, ex situ electrolyte spreading measurements were carried out on three different 10C-1.5O samples. The cation migration on the three samples was stopped after 10, 20, and 30 h, and XPS measurements were carried out to calculate the cation concentration. As depicted in Fig. 12b, the concentration of cations in the migrated regions kept decreasing with increasing times, ascertaining the counter migration of hydroxide ions towards the defect. Since the main task of cation migration is to decrease the potential at the front, which can be considered as cation insertion into the intact area¹⁰. This might lead to a decrease in concentration with time if no further cations are supplied.

The lower concentration of cations on thicker Cr–O layers is explained by the lower capacitance of that surface. Electrons flow parallel along the surface (if there is an insulating layer, under the oxide), cation migrate with them on the surface. The oxide layer with cations on the surface and electrons on the other side (oxide/metal interface), can be considered as a capacitor with opposite

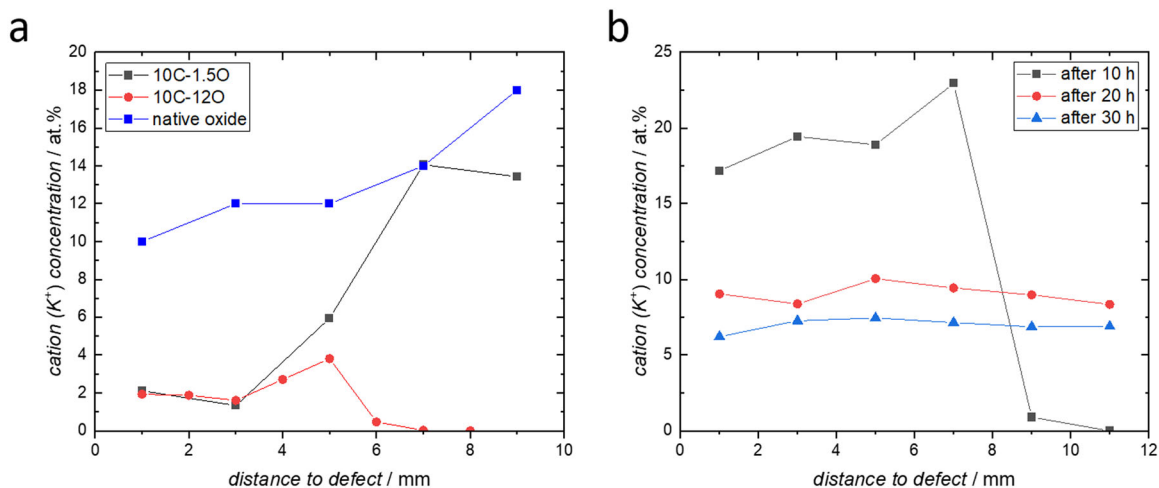


Fig. 12 Cation concentrations on the surface from XPS. Concentration of potassium on the surface obtained using XPS from various locations on **a** the samples 10C-1.5O, 10C-12O (after allowing cathodic spreading to continue ex situ following the SKP measurements in Fig. 5c) and chromium with native oxide after cation migration measurements, and **b** the sample 10C-1.5O measured at different times after commencement of electrolyte spreading.

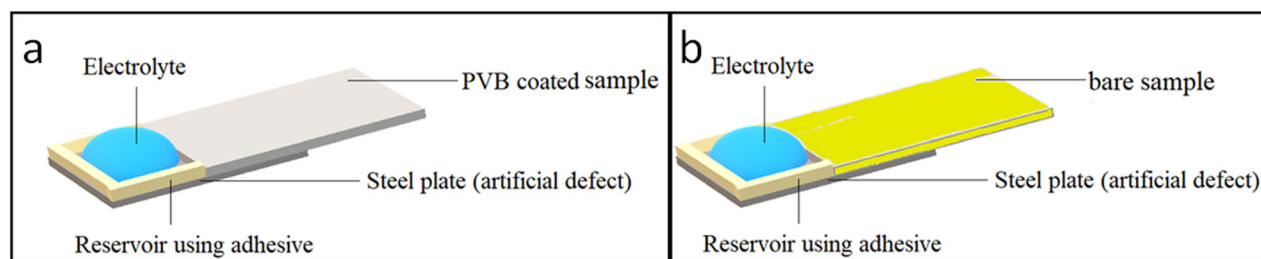


Fig. 13 Sample model. Model of sample used to study **a** Cathodic delamination with phenolphthalein incorporated in PVB and **b** in situ cathodic electrolyte spreading with Scanning Kelvin probe.

charges on the two sides/surfaces. The thicker the insulating oxide, the lower the surface capacity, i.e., the lower the necessary amount migrating cations to pull down the potential. Therefore, the thicker oxide would require a lower amount of charge than the thinner oxide layer to lower the potential by the same amount on both the layers, resulting in a lower concentration of cations at the migration front. However, one would expect, if you have a thicker insulating oxide, progress of the migration front should be even faster due to the lower amount of charges required to pull down the potential. However, we observe that the rate of cation migration is much lower on the 10C-12O sample (Figs. 5c and 6). This underlines the highly hindered cation migration on the Cr-O surfaces¹⁰.

To summarize, the kinetics of oxygen reduction induced electrolyte spreading on the different chromium-oxide-terminated samples investigated here, was found to be comparable to the delamination kinetics of organic coatings of polyvinylbutyral polymer on the samples. The electrical conductivity of such chromium-coated steels (comprising Cr-O-C and Cr-O layers) electrodeposited from trivalent chromium electrolyte was investigated using current-sensing atomic force microscopy and the cathodic electrolyte spreading on the surface of these coatings was studied using in situ scanning Kelvin probe and scanning Kelvin probe force microscopy. The concentration of cationic species on the surface of the samples after electrolyte spreading was analyzed using X-ray photoelectron spectroscopy. The following outcomes can be deduced:

1. The sample with a 12 nm Cr-O layer resisted current flow at very high applied bias, showing leakage current only at tiny defects in the layer. The resistance was even higher than for the standard ECCS coating. On the contrary, the sample with a 1.5 nm Cr-O layer exhibited distinct conductive and non-conductive regions characteristic of the native oxide and Cr-O layer, respectively.
2. The oxygen-deficient oxide in the Cr-O layer behaves like an n-type semiconductor with a wide band-gap. The electron transport in the Cr-O layer is highly inhibited compared to the native oxide layer on chromium. The inhibited electron transfer by the Cr-O layer was also supported by lack of coloration of phenolphthalein in the delaminated area of delaminating PVB coatings with phenolphthalein additions, which would otherwise occur due to the formation of hydroxide ions during oxygen reduction reaction.
3. In situ scanning Kelvin probe force microscopy during electrolyte spreading revealed heterogeneity on the surface of both 12 nm and 1.5 nm Cr-O-coated samples. The heterogeneity in the thinner Cr-O-coated sample arises from the native oxide formed at locations where the Cr-O is not deposited. These locations act as preferred sites of oxygen reduction, hence result in predominant cation migration and reduction of potential. It was also observed that in the initial stage of migration, cation migration may also occur against the electric field, i.e., the gradient of the whole electrochemical potential needs to be considered as driving force.

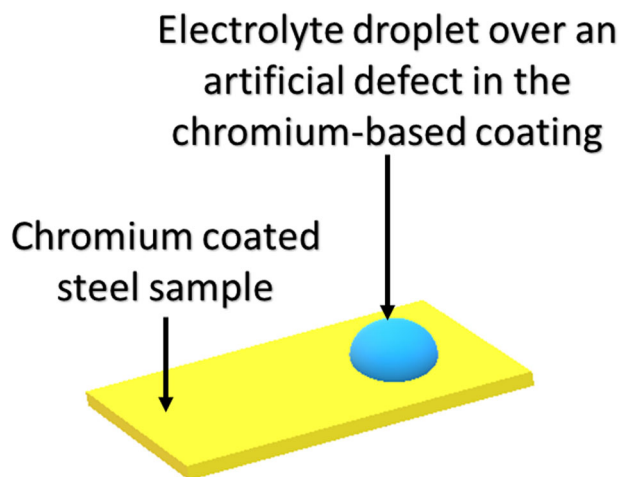


Fig. 14 Sample model. Model of sample used to study in situ electrolyte spreading with scanning Kelvin probe force microscopy.

4. The non-conductive Cr–O layer prevents electron transfer for oxygen reduction and shows a high resistance for cation migration. Heterogeneity on the 12 nm Cr–O sample arises due to slightly defective areas in the coatings. These defects act as preferred locations for electron transfer, and also are proposed to feature a higher mobility for the cations. The low capacitance of the thick Cr–O layer explains the lower concentration of cationic species on the surface after the spreading of the electrolyte.
5. The electrolyte spreading on the surface of the chromium-coated steels was monitored in situ using highly resolved scanning Kelvin probe force microscopy. The kinetics of the spreading observed was similar to the kinetics observed on a larger scale using the scanning Kelvin probe. A clear front distinguishing the cation migrated regions from the non-migrated regions was observed for the 12 nm Cr–O sample where the cation migration is slower than for the 1.5 nm Cr–O sample, where the front was observed to be smeared out over a larger area than could be covered by SKPFM. The results indicate that on the microscopic scale progress of cathodic spreading (and hence also cathodic delamination) is not homogeneous, i.e., it is faster in some areas than in others, but the overall macroscopically observed rate is determined by the slowest progress rate at the microscopic scale.

METHODS

Chromium coatings electrodeposited from trivalent chromium electrolyte (TCCT)

The steel samples coated with the chromium-based coatings consisting of two layers, a mixed Cr–O–C base layer covered with an oxygen-rich Cr–O topcoat, were obtained from Tata Steel Packaging Europe. The details regarding the production conditions and characterization of the samples are described elsewhere⁵. The thickness of the Cr–O–C layer is 10 nm in both the chromium-coated samples used in this study (10C-1.50 and 10C-120). The thickness of the Cr–O topcoat on the 10C-1.50 and 10C-120 samples is 1.5 nm and 12 nm, respectively⁵. Pure chromium samples of 0.5 mm thickness and 99.99% purity were procured from Goodfellow, Germany. Samples of chromium coating electrodeposited from hexavalent chromium electrolyte (ECCS) were also obtained from Tata Steel Packaging Europe.

Current-sensing atomic force microscopy studies

The CS-AFM measurements were performed with a Keysight 9500 Atomic Force Microscope combined with the NanoNavigator software. The current-sensing measurements are carried out in the contact mode of

the AFM. Electrically conductive diamond-coated CDT-CONTR tips obtained from Nanosensors™ were used. Dry nitrogen gas was purged into the environmental cell to maintain a low relative humidity of 12–15% RH. Current maps were obtained by applying a DC voltage across the sample and raster scanning the tip across a 50 × 50 μm area on the surface. The topography and the current at a location are mapped simultaneously. The current maps were obtained from at least three different locations on each sample to check for repeatability. *I*–*V* sweeps are performed in the spectroscopy mode of the NanoNavigator software. *I*–*V* curves were obtained by sweeping the applied bias voltage from –10 to 10 V within a duration of 5 s. *I*–*V* sweeps were performed at five different locations on the samples and at least three times at each location, and were found to be reproducible at each location. The data obtained during the measurements were processed using the Pico Image analysis software.

Observations with phenolphthalein

Visual observations were carried out during cathodic delamination of model polyvinyl-butylal (PVB) polymer coatings (10 wt.% PVB polymer in ethanol), by dissolving phenolphthalein (0.2 mol/L) in the PVB solution. The PVB solution containing the pH indicator was coated on the surface of the sample with a spin coater and dried in a furnace preheated to 80 °C for 10 min. The PVB-coated sample was then placed in contact with a 1 M KCl electrolyte reservoir on a steel sample (as depicted in Fig. 13a), which acts as an artificial defect in the coating. The walls of the reservoir were formed using X60 adhesive. The sample in contact with the reservoir was placed in a humidity chamber to prevent drying of electrolyte. ORR occurring on the surface of the sample underneath the PVB leads to an alkaline shift in pH, which leads to the violet coloration of phenolphthalein. The visual changes were observed at different time intervals and photographs were obtained.

Scanning Kelvin probe measurements

The evolution of potential profiles associated with the spreading of the electrolyte on the surface of the samples was studied using SKP. The samples were cut into sheets of dimension 20 × 20 mm and placed in contact with a 1 M KCl reservoir on a steel plate, which acts as an artificial defect. A reservoir using X60 cold curing adhesive was prepared on the steel plate, to accommodate the electrolyte (as shown in Fig. 13b). The setup containing the sample and the reservoir was placed in the SKP chamber to perform in situ electrolyte spreading measurements. The SKP chamber was maintained at high relative humidity (RH > 93%) by purging humid air through an external humidification setup. The corrosion potential of the sample surface can be obtained from the Volta potential difference measured in the SKP technique, it differs just by an offset value, which needs to be determined prior to the measurement^{58–60}. The Ni–Cr tip employed in the SKP was calibrated using saturated CuSO₄ in a copper crucible as a Cu/CuSO₄ standard electrode. After calibration, the corrosion potential measurements were recorded and reported against the standard hydrogen electrode (SHE).

Scanning Kelvin probe force microscopy measurements

SKPFM measurements were carried out with an Asylum Research Cypher ES–Environmental AFM, with environmental control capability. During the measurements, a two-pass raster scan is carried out at each line, with the recording of topography in the first pass and contact potential difference in the second ‘nap’ pass. During the nap pass, the tip is lifted to a predefined height (50 nm in this study) to measure the potentials. Conductive Ti–Ir-coated Si tips–ASYLEEC.01-R2 procured from Oxford instruments were used to carry out in situ SKPFM measurements during electrolyte spreading. An artificial defect was created by scratching a small area of the chromium-based coating to expose the steel underneath. 1 M KCl electrolyte droplet of 1 μL volume was placed on the created defect using a micropipette (as shown in Fig. 14). The relative humidity was maintained at >90% RH by purging the cell with humidified oxygen, flowing through an external humidification setup. The potential maps were obtained using a scan rate of 1 Hz, to follow the swiftly moving migration front. The time taken to capture each frame of the potential map was ~8 min. The output potential signal obtained from the SKPFM is to be inverted to obtain the actual Volta potential of the surface^{61–64}. All the surface Volta potentials reported here are after reversal of polarity of the obtained values.

XPS studies

XPS survey spectra were acquired on a Physical Electronics PHI Quantera II spectrometer using Al-K_α source at 1486.6 eV, energy step size of 0.25 eV, and a pass energy of 59 eV. A take-off angle of 45° was used during the measurements. The quantification of the survey spectra was carried out in CasaXPS software version 2.3.22, using a Shirley-type background for the quantified regions.

DATA AVAILABILITY

The datasets generated and/or analyzed during the current study are available from the corresponding author on reasonable request.

Received: 6 April 2022; Accepted: 18 August 2022;

Published online: 06 September 2022

REFERENCES

- Kwon, S. C. et al. Characterization of intermediate Cr-C layer fabricated by electrodeposition in hexavalent and trivalent chromium baths. *Surf. Coat. Technol.* **183**, 151–156 (2004).
- Protsenko, V. S., Kityk, A. A. & Danilov, F. I. Kinetics and mechanism of chromium electrodeposition from methanesulfonate solutions of Cr(III) salts. *Surf. Eng. Appl. Electrochem.* **50**, 384–389 (2014).
- Protsenko, V. S. & Danilov, F. I. Chromium electroplating from trivalent chromium baths as an environmentally friendly alternative to hazardous hexavalent chromium baths: comparative study on advantages and disadvantages. *Clean. Technol. Environ. Policy* **16**, 1201–1206 (2014).
- Wijenberg, J. H. O. J., Steegh, M., Aarnts, M. P., Lammers, K. R. & Mol, J. M. C. Electrodeposition of mixed chromium metal-carbide-oxide coatings from a trivalent chromium-formate electrolyte without a buffering agent. *Electrochim. Acta* **173**, 819–826 (2015).
- Prabhakar, J. M. et al. Chromium coatings from trivalent chromium plating baths: Characterization and cathodic delamination behaviour. *Corros. Sci.* **187**, 109525 (2021).
- Warren, D. J., McMurray, H. N. & de Vooy, A. C. A. Localised SKP studies of cathodic disbondment on chromium/chromium oxide coated steel. *ECS Trans.* **50**, 67–78 (2013).
- Wint, N., Warren, D. J., DeVooy, A. C. A. & McMurray, H. N. The use of chromium and chromium (III) oxide PVD coatings to resist the corrosion driven coating delamination of organically coated packaging steel. *J. Electrochem. Soc.* **167**, 141506 (2020).
- Wint, N., de Vooy, A. C. A. & McMurray, H. N. The corrosion of chromium based coatings for packaging steel. *Electrochim. Acta* **203**, 326–336 (2016).
- Edy, J. E., McMurray, H. N., Lammers, K. R. & deVooy, A. C. A. Kinetics of corrosion-driven cathodic disbondment on organic coated trivalent chromium metal-oxide-carbide coatings on steel. *Corros. Sci.* **157**, 51–61 (2019).
- Prabhakar, J. M., Kerger, P., de Vooy, A. & Rohwerder, M. Migration of ions on oxygen-deficient chromium oxide electrodeposited from trivalent chromium electrolyte. *Corros. Sci.* **199**, 110185 (2022).
- Williams, G., Kousis, C., McMurray, N. & Keil, P. A mechanistic investigation of corrosion-driven organic coating failure on magnesium and its alloys. *NPJ Mater. Degrad.* **3**, 41 (2019).
- Wijenberg, J. H. O. J., Wittebrood, A. J. & Litz, M. W. *Method For Manufacturing Chromium-Chromium Oxide Coated Blackplate. European Patent EP3728701* (2019).
- Posner, R., Fink, N., Wolpers, M. & Grundmeier, G. Electrochemical electrolyte spreading studies of the protective properties of ultra-thin films on zinc galvanized steel. *Surf. Coat. Technol.* **228**, 286–295 (2013).
- Qian, J., Liao, S., Xu, S., Strosio, M. A. & Dutta, M. Direct measurement of electrical transport through single DNA molecules. *J. Appl. Phys.* **106**, 033702 (2009).
- Souier, T., Martin, F., Bataillon, C. & Cousty, J. Local electrical characteristics of passive films formed on stainless steel surfaces by current sensing atomic force microscopy. *Appl. Surf. Sci.* **256**, 2434–2439 (2010).
- Yakubov, V., Lin, M., Volinsky, A. A., Qiao, L. & Guo, L. The hydrogen-induced pitting corrosion mechanism in duplex stainless steel studied by current-sensing atomic force microscopy. *NPJ Mater. Degrad.* **2**, 1–4 (2018).
- Guo, L. Q., Lin, M. C., Qiao, L. J. & Volinsky, A. A. Duplex stainless steel passive film electrical properties studied by in situ current sensing atomic force microscopy. *Corros. Sci.* **78**, 55–62 (2014).
- Helou, M. El. *Organic-Inorganic Semiconductor Hybrid Systems: Structure, Morphology, and Electronic Properties*. (Philipps-Universität Marburg, 2012).
- Alpers, B., Rubinstein, I. & Hodes, G. Identification of surface states on individual CdSe quantum dots by room-temperature conductance spectroscopy. *Phys. Rev. B Condens. Matter Mater. Phys.* **63**, 1–4 (2001).
- Alpers, B., Cohen, S., Rubinstein, I. & Hodes, G. Room-temperature conductance spectroscopy of CdSe quantum dots using a modified scanning force microscope. *Phys. Rev. B* **52**, 17–20 (1995).
- Neufeld, A. K., Cole, I. S., Bond, A. M. & Furman, S. A. The initiation mechanism of corrosion of zinc by sodium chloride particle deposition. *Corros. Sci.* **44**, 555–572 (2002).
- Chen, Z. Y., Persson, D. & Leygraf, C. Initial NaCl-particle induced atmospheric corrosion of zinc-Effect of CO₂ and SO₂. *Corros. Sci.* **50**, 111–123 (2008).
- Tsuru, T., Tamiya, K. I. & Nishikata, A. Formation and growth of micro-droplets during the initial stage of atmospheric corrosion. *Electrochim. Acta* **49**, 2709–2715 (2004).
- Chen, Z. Y. et al. In situ studies of the effect of CO[sub 2] on the initial NaCl-induced atmospheric corrosion of copper. *J. Electrochem. Soc.* **152**, B342 (2005).
- Nazarov, A., Le Bozec, N. & Thierry, D. Assessment of steel corrosion and delamination of epoxy barrier paint by scanning Kelvin probe. *Prog. Org. Coat.* **114**, 123–134 (2018).
- Zhong, X. et al. Limiting current density of oxygen reduction under ultrathin electrolyte layers: from the micrometer range to monolayers. *ChemElectroChem* **8**, 712–718 (2021).
- Posner, R., Titz, T., Wapner, K., Stratmann, M. & Grundmeier, G. Transport processes of hydrated ions at polymer/oxide/metal interfaces. Part 2. Transport on oxide covered iron and zinc surfaces. *Electrochim. Acta* **54**, 900–908 (2009).
- Posner, R., Wapner, K., Stratmann, M. & Grundmeier, G. Transport processes of hydrated ions at polymer/oxide/metal interfaces. Part 1. Transport at interfaces of polymer coated oxide covered iron and zinc substrates. *Electrochim. Acta* **54**, 891–899 (2009).
- Nazarov, A., Diler, E., Persson, D. & Thierry, D. Electrochemical and corrosion properties of ZnO/Zn electrode in atmospheric environments. *J. Electroanal. Chem.* **737**, 129–140 (2015).
- Vacandio, F. et al. New knowledge on localized corrosion obtained from local measuring techniques. *Electrochim. Acta* **46**, 3641–3650 (2001).
- Leblanc, P. P. & Frankel, G. S. Investigation of filiform corrosion of epoxy-coated 1045 carbon steel by scanning kelvin probe force microscopy. *J. Electrochem. Soc.* **151**, B105 (2004).
- Senöz, C. & Rohwerder, M. Scanning Kelvin probe force microscopy for the in situ observation of the direct interaction between active head and intermetallic particles in filiform corrosion on aluminium alloy. *Electrochim. Acta* **56**, 9588–9595 (2011).
- Wint, N. et al. The kinetics and mechanism of filiform corrosion occurring on zinc-aluminium-magnesium coated steel. *Corros. Sci.* **158**, 108073 (2019).
- Rohwerder, M., Hornung, E. & Stratmann, M. Microscopic aspects of electrochemical delamination: an SKPFM study. *Electrochim. Acta* **48**, 1235–1243 (2003).
- Örnek, C., Leygraf, C. & Pan, J. Passive film characterisation of duplex stainless steel using scanning Kelvin probe force microscopy in combination with electrochemical measurements. *NPJ Mater. Degrad.* **3**, 1–8 (2019).
- Sun, B., Zuo, X., Cheng, X. & Li, X. The role of chromium content in the long-term atmospheric corrosion process. *NPJ Mater. Degrad.* **4**, 1–9 (2020).
- Senöz, C., Borodin, S., Stratmann, M. & Rohwerder, M. In situ detection of differences in the electrochemical activity of Al₂Cu IMPs and investigation of their effect on FFC by scanning Kelvin probe force microscopy. *Corros. Sci.* **58**, 307–314 (2012).
- Rozhok, S., Sun, P., Piner, R., Lieberman, M. & Mirkin, C. A. AFM study of water meniscus formation between an AFM tip and NaCl substrate. *J. Phys. Chem. B* **108**, 7814–7819 (2004).
- Weeks, B. L., Vaughn, M. W. & Deyoreo, J. J. Direct imaging of meniscus formation in atomic force microscopy using environmental scanning electron microscopy. *Langmuir* **21**, 8096–8098 (2005).
- Mandich, N. V. & Snyder, D. L. Electrodeposition of Chromium. in *Modern Electroplating* (ed. Mordechai Schlesinger, M. P.) vol. 73, 205–248 (John Wiley & Sons, Inc., 2011).
- Moore, J. C., Kenny, S. M., Baird, C. S., Morkoç, H. & Baski, A. A. Electronic behavior of the Zn- and O-polar ZnO surfaces studied using conductive atomic force microscopy. *J. Appl. Phys.* **105**, 116102 (2009).
- Guo, L. Q., Qin, S. X., Yang, B. J., Liang, D. & Qiao, L. J. Effect of hydrogen on semiconductive properties of passive film on ferrite and austenite phases in a duplex stainless steel. *Sci. Rep.* **7**, 1–6 (2017).
- Rumler, M. et al. Characterization of grain boundaries in multicrystalline silicon with high lateral resolution using conductive atomic force microscopy. *J. Appl. Phys.* **112**, 034909 (2012).
- Kiselev, V. F. & Krylov, O. V. *Adsorption and Catalysis on Transition Metals and Their Oxides*. Vol. 9 (Springer, 1989).

45. Greiner, M. T. & Lu, Z. H. Thin-film metal oxides in organic semiconductor devices: Their electronic structures, work functions and interfaces. *NPG Asia Mater.* **5**, 1–16 (2013).
46. Leng, A., Streckel, H. & Stratmann, M. The delamination of polymeric coatings from steel. Part 2: First stage of delamination, effect of type and concentration of cations on delamination, chemical analysis of the interface. *Corros. Sci.* **41**, 579–597 (1998).
47. Parks, G. A. The isoelectric points of solid oxides, solid hydroxides, and aqueous hydroxo complex systems. *Chem. Rev.* **65**, 177–198 (1965).
48. Kosmulski, M. Isoelectric points and points of zero charge of metal (hydr)oxides: 50 years after Parks' review. *Adv. Colloid Interface Sci.* **238**, 1–61 (2016).
49. Khayatan, N. & Rohwerder, M. A new insight into the rate determining step of cathodic delamination. *Corros. Sci.* **202**, 110311 (2022).
50. Wielant, J., Posner, R., Hausbrand, R., Grundmeier, G. & Terryn, H. SKP as a tool to study the physicochemical interaction at buried metal-coating interfaces. *Surf. Interface Anal.* **42**, 1005–1009 (2010).
51. Salgin, B., Özkanat, Ö., Mol, J. M. C., Terryn, H. & Rohwerder, M. Role of surface oxide properties on the aluminum/epoxy interfacial bonding. *J. Phys. Chem. C.* **117**, 4480–4487 (2013).
52. Leng, A., Streckel, H., Hofmann, K. & Stratmann, M. The delamination of polymeric coatings from steel Part 3: effect of the oxygen partial pressure on the delamination reaction and current distribution at the metal/polymer interface. *Corros. Sci.* **41**, 599–620 (1998).
53. Stratmann, M. et al. The scanning Kelvin probe; a new technique for the in situ analysis of the delamination of organic coatings. *Prog. Org. Coat.* **27**, 261–267 (1996).
54. Hausbrand, R., Stratmann, M. & Rohwerder, M. Delamination resistant zinc alloys: simple concept and results on the system zinc-magnesium. *Steel Res. Int.* **74**, 453–458 (2003).
55. Hausbrand, R., Stratmann, M. & Rohwerder, M. The physical meaning of electrode potentials at metal surfaces and polymer/metal interfaces: consequences for delamination. *J. Electrochem. Soc.* **155**, C369 (2008).
56. Rohwerder, M. In *Encyclopedia of Interfacial Chemistry*. 414–422 (Elsevier, 2018).
57. Shkirskiy, V. et al. Cathodic driven coating delamination suppressed by inhibition of cation migration along Zn|polymer interface in atmospheric CO₂. *NPJ Mater. Degrad.* **3**, 1–10 (2019).
58. Leng, A., Streckel, H. & Stratmann, M. The delamination of polymeric coatings from steel. Part 1: calibration of the kelvinprobe and basic delamination mechanism. *Corros. Sci.* **41**, 547–578 (1998).
59. Uebel, M. et al. Fabrication of robust reference tips and reference electrodes for kelvin probe applications in changing atmospheres. *Langmuir* **33**, 10807–10817 (2017).
60. Ehahoun, H., Stratmann, M. & Rohwerder, M. Ag/AgCl/KCl micro-electrodes as O₂-insensitive reference tips for dynamic scanning Kelvin probe measurement. *Electrochim. Acta* **50**, 2667–2674 (2005).
61. Rohwerder, M. & Turcu, F. High-resolution Kelvin probe microscopy in corrosion science: scanning Kelvin probe force microscopy (SKPFM) versus classical scanning Kelvin probe (SKP). *Electrochim. Acta* **53**, 290–299 (2007).
62. Schmutz, P. & Frankel, G. S. Characterization of AA2024-T3 by Scanning Kelvin Probe Force Microscopy. *J. Electrochem. Soc.* **145**, 2285–2295 (1998).
63. Revilla, R. I., Terryn, H. & De Graeve, I. On the use of SKPFM for in situ studies of the repassivation of the native oxide film on aluminium in air. *Electrochem. Commun.* **93**, 162–165 (2018).
64. Cook, A. B. B. et al. Calibration of the scanning Kelvin probe force microscope under controlled environmental conditions. *Electrochim. Acta* **66**, 100–105 (2012).

ACKNOWLEDGEMENTS

This work is funded by Tata Steel, Ijmuiden through IMPRS-SurMat program.

AUTHOR CONTRIBUTIONS

J.M. carried out the experiments, analysis, and interpretation of the data. J.M. wrote the paper. All authors contributed to the proof reading. A.V. provided the samples and supervised the project. M.R. conceptualized the project, acquired funding, supervised, and coordinated the project.

FUNDING

Open Access funding enabled and organized by Projekt DEAL.

COMPETING INTERESTS

The authors declare no competing interests.

ADDITIONAL INFORMATION

Supplementary information The online version contains supplementary material available at <https://doi.org/10.1038/s41529-022-00285-7>.

Correspondence and requests for materials should be addressed to J. Manoj Prabhakar.

Reprints and permission information is available at <http://www.nature.com/reprints>

Publisher's note Springer Nature remains neutral with regard to jurisdictional claims in published maps and institutional affiliations.



Open Access This article is licensed under a Creative Commons Attribution 4.0 International License, which permits use, sharing, adaptation, distribution and reproduction in any medium or format, as long as you give appropriate credit to the original author(s) and the source, provide a link to the Creative Commons license, and indicate if changes were made. The images or other third party material in this article are included in the article's Creative Commons license, unless indicated otherwise in a credit line to the material. If material is not included in the article's Creative Commons license and your intended use is not permitted by statutory regulation or exceeds the permitted use, you will need to obtain permission directly from the copyright holder. To view a copy of this license, visit <http://creativecommons.org/licenses/by/4.0/>.

© The Author(s) 2022